

35 **Abstract**

36

37 Projections from the substantia nigra and striatum traverse through the pallidum on the

38 way to their targets. To date, in vivo characterization of these pathways remains elusive.

39 Here we used high angular resolution diffusion imaging (N=138) to study the

40 characteristics and structural subcompartments of the human pallidum. Our results

41 show that the diffusion orientation distribution at the pallidum is asymmetrically oriented

42 in a dorsolateral direction, consistent with the orientation of underlying fiber systems.

43 Furthermore, compared to the outer pallidal segment, the internal segment has more

44 peaks in the orientation distribution function and stronger anisotropy in the primary fiber

45 direction, consistent with known cellular differences between the underlying nuclei.

46 These differences in orientation, complexity, and degree of anisotropy are sufficiently

47 robust to automatically segment the pallidal nuclei using diffusion properties. Thus the

48 gray matter diffusion signal can be useful as an in vivo measure of the collective

49 nigrostriatal and striatonigral pathways.

50 Keywords: basal ganglia, diffusion imaging, nigrostriatal, striatonigral, globus pallidus

51 **Introduction**

52 The basal ganglia are a crucial forebrain network associated with many cognitive
53 functions, including reward processing, decision-making, and learning (Hollerman et al.,
54 2000; Haber, 2003). Many aspects of basal ganglia function rely on dopaminergic
55 inputs from the substantia nigra that serve as a modulatory signal for neurons in the
56 subpallium (Haber et al., 2000). These dopaminergic inputs are conducted by a set of
57 fiber bundles that originate in the pars compacta region of the substantia nigra, a portion
58 of which migrate in a dorsolateral direction through the segments of the globus pallidus
59 (Carpenter and Peter, 1972). While a majority of these projections pass through the
60 pallidum and terminate on cells in the striatal nuclei (Carpenter and McMasters, 1964), a
61 significant number of them also terminate in the inner and outer segments of the globus
62 pallidus, forming the nigropallidal pathway (Cossette et al., 1999). Two other major fiber
63 systems traversing through the globus pallidus project from the striatum, including the
64 striatopallidal fiber systems, which form the canonical direct and indirect pathways, and
65 the striatonigral fiber system. Breakdowns in these various pathways form the etiology
66 of several neurodegenerative diseases. For example, axonal degeneration of the
67 nigrostriatal pathway is the pathological hallmark of Parkinson's Disease (Burke and
68 O'Malley, 2013) while Huntington's disease is characterized by a loss of medium spiny
69 neurons within the striatum that project to the globus pallidus (Reiner et al., 1988). Thus
70 *in vivo* characterization of these basal ganglia projections has clear clinical implications.
71

72 One problem with characterizing both the nigral and striatal efferents is that they are
73 largely embedded within the gray matter of several basal ganglia nuclei, primarily within
74 the globus pallidus. The globus pallidus is the primary output of the basal ganglia
75 network, sending projections that relay signals from upstream nuclei to the thalamus
76 (Alexander et al., 1986). In primates it is comprised of an external segment (GPe),
77 which serves as an inhibitory relay nucleus within the indirect pathway, and the internal
78 segment (GPi) that aggregates all information from all basal ganglia pathways. While
79 primarily defined by their connectivity and neurophysiological profiles, the GPe and GPi
80 are also distinguishable at the cellular level by differences in cell density, cell type, and
81 morphology (Hardman et al., 2002, Eid et al 2013, Difiglia and Rafols, 1988). One of
82 the most salient differences is that the GPi has a much lower overall neuronal density
83 (see table 2 in Hardman et al., 2002). More importantly, given that the volume of the GPi
84 is smaller than that of the GPe and that both nigrostriatal and striatonigral fibers pass
85 through the globus pallidus on their way to their targets, the GPi also has a greater
86 density of both nigrostriatal and striatonigral efferents than its external counterpart.
87
88 Despite the clear morphological differences, in vivo characterization of these critical
89 nuclei remains elusive by MRI-based neuroimaging technologies, particularly with
90 conventional T1-weighted or T2-wighted images used in most human neuroimaging
91 experiments. This is because T1-weighted and T2-weighted approaches have limited
92 power to characterize the microscopic structure of the GPe and the GPi. This limitation
93 can be compensated by the recent advances in high angular resolution diffusion MRI,

94 which offers a non-invasive approach to study microscopic structure. One advantage of
95 diffusion MRI is that it is able to detect microscopic differences in underlying cellular
96 morphologies, including spatial asymmetry in underlying axonal tracts, and it has shown
97 great promise in quantifying variability in underlying tissue composition (Behrens et al.,
98 2003). With these unique features, diffusion MRI has emerged as an increasingly
99 popular tool for characterizing the neural tissues (Abhinav et al., 2014). While most
100 commonly used to study structural subcomponents of large white matter fascicles
101 (Bastiani, 2012, Wang et al, 2013, Fernandez-Miranda 2014), diffusion MRI has also
102 been shown to be useful for characterizing differences in microstructural cellular
103 properties of gray matter (Wiegell et al., 2003; Mang et al., 2012), including sensitivity to
104 both neural and glial distribution patterns (Blumenfeld-Katzir et al., 2011). For example,
105 analysis of the diffusion MRI signal has been used to segment the different thalamic
106 nuclei in humans (Behrens et al, 2003).

107

108 Here we adopt an atlas approach to study the orientation distribution functions of the
109 water diffusion, termed spin distribution functions (SDF; Yeh et al. 2010) within the gray
110 matter of the globus pallidus in a stereotaxic space. An SDF provides a nonparametric
111 representation of the diffusion pattern that cannot be offered by conventional tensor-
112 based analysis, thus allowing for characterizing and segmenting structural
113 subcomponents. Here we used data from two high angular resolution diffusion
114 sequences, diffusion spectrum imaging (DSI) and multi-shell imaging (MSI) and
115 examined the diffusion characteristics in the nigral and striatal efferents. We also

116 examined whether there are reliable differences in the SDFs between the GPe and the
117 GPi that allows for accurate segmentation based solely on diffusion properties. These
118 findings may identify a clear potential for using high angular resolution diffusion MRI as
119 a novel *in vivo* characterization of the microarchitecture of the human globus pallidus,
120 including the nigral and striatal efferents that break down in various neurological
121 pathologies.

122

123 **Results**

124 Dorsolateral orientation of the pallidal diffusion signal

125 The nigrostriatal and striatonigral fibers traverse the pallidum on the way to their targets,
126 resulting in a primarily dorsolateral-ventromedial orientation of the collective axons (Fig.
127 1A). In humans, the two segments of the pallidum are separated by a thin white matter
128 band, called the internal medullary lamina, shown in coronal sections from the Big Brain
129 atlas in Fig.1B and 1C (Amunts et al., 2013). To characterize the orientations of the
130 fibers in the inner and outer segment of the globus pallidus, we isolated the voxels
131 corresponding to the two segments (Methods, Fig 2A). Within each of these region
132 masks we estimated the SDFs from the diffusion signal of each voxel (Fig 2B-D), which
133 is a 3D representation of the underlying diffusion orientation distribution. The first three
134 peaks in each SDF were extracted and their orientation and anisotropy intensity, called
135 quantitative anisotropy (QA; Fig. 2B, see Methods), were recorded for every voxel in
136 each mask. Two representative SDFs from an example subject from the DSI dataset

137 show how the shapes of the SDFs differ between the inner (Fig. 2C) and outer (Fig. 2D)
138 segments of the pallidum.

139

140 Figure 3 shows the distribution of principal fiber angles across subjects in the DSI and
141 MSI samples. Each distribution was confirmed to be non-uniform using a Rayleigh's
142 test (z values > 36.12 , p -values < 0.001) and exhibited consistent peaks in the
143 orientations in the fibers in both region masks and both data samples. In both the DSI
144 and MSI samples, the distribution of the angles in the inner segment is predominately
145 concentrated in the dorsolateral direction, consistent with the known orientation of the
146 major nigral and striatal efferents (Wilson 1914, Szabo 1967, Szabo 1962, Fox and
147 Rafols, 1976, Carpenter and Peter 1972). Compared to the inner segment, the
148 distribution of the angles in the outer segment is rotated medially, clockwise in the left
149 hemisphere and anticlockwise in the right hemisphere. Interestingly, this rotation is more
150 pronounced in the DSI dataset, resulting in the majority of fibers pointing dorsomedially
151 (towards the internal capsule). One possibility is that the predominantly dorsal and
152 dorsolateral fiber systems are not contributing to the strongest anisotropy pattern in the
153 DSI sample, but are still present at lower anisotropy thresholds. To explore this, we
154 looked at the orientation of the secondary fibers in both datasets (Fig. 4). Indeed, the
155 secondary fiber in the DSI dataset was oriented in a more dorsolateral direction as
156 predicted if it were reflecting the angle of the underlying nigral and striatal efferents (red
157 histogram in Fig. 4 A,B).

158

159 These patterns of fiber peak orientations within the SDF are also clearly visible in the
160 geometries of the extracted fibers at each voxel. Figure 5 shows a coronal slice from
161 two representative subjects from the DSI and MSI samples. A majority of the primary
162 and secondary fibers overlap in the inner segment (blue voxels) and are generally
163 oriented dorsolaterally, whereas the primary and secondary fibers in the external
164 segment (red voxels) show less overlap and exhibit a greater abundance of dorsomedial
165 orientations compared to the internal segment. Thus, the gray matter diffusion signal
166 within the pallidal nuclei has asymmetries in peak anisotropy directions that are
167 consistent with the orientation of nigral and striatal efferents running through the
168 pallidum, suggesting that the diffusion signal is sensitive to these underlying pathways.

169

170 Differential diffusion patterns between inner & outer pallidal segments

171 Along with differences in fiber orientation, we also observed general differences in the
172 sensitivity and intensity of the diffusion signal between the two pallidal segments.
173 Tensor-based analyses have shown that the anisotropy patterns around the principal
174 fiber direction tend to be highly sensitive to underlying cellular morphology differences
175 (Wiegell et al., 2003). Figure 6, panels A through D, shows the across-subject
176 probability distributions of the mean QA in the principal fiber direction, for both pallidal
177 segments. The peaks (arrows) of the distributions occurred at consistently higher
178 thresholds in the inner segment in both hemispheres and both samples. Thus, the inner
179 segment exhibited a mean shift in QA compared to the outer segment mask, suggesting
180 a slightly stronger diffusion intensity for the inner pallidal segment.

181
182 Differences between the pallidal segments were also reflected in the complexity of the
183 SDF geometry. The sensitivity curves in Figure 6, panels E through H, show the
184 average number of resolved fibers (y-axis) with QA values above the value shown on
185 the x-axis. Thus this measures the complexity of the diffusion geometry in each voxel by
186 showing the robustness of the fiber peaks within the reconstructed SDF across a range
187 of thresholds. As expected, the number of resolved fibers decays rapidly as the
188 threshold increases. Notably, compared to the outer segment, in the DSI sample we
189 detected more fibers in the inner segment at thresholds less than $QA = 0.05$ (Fig.6 E,F),
190 and more fibers in the outer segment at thresholds higher than 0.05. In the MSI sample,
191 these distributions largely overlapped (Fig.6 G,H), although the inner segment in the
192 right hemisphere showed a smaller shift in the same direction as was observed in the
193 DSI dataset. Taken together, the differences in orientation, intensity and sensitivity
194 between the structures suggest that the diffusion signal is picking up on reliable
195 differences in the cellular content of the two nuclei.

196

197 Reliable segmentation of pallidal nuclei

198 If these differences are reflecting distinctive cellular architectures and local connectivity
199 patterns then it should be possible to classify the two segments based purely on the
200 properties of the DWI signal. To this end we used k-means clustering to segment all
201 voxels within the globus pallidus using three voxel features as inputs: principle fiber
202 orientation, anisotropy of the peak fiber, and number of detected fibers. Based on these

203 properties alone, we generated probabilistic maps of the inner and outer segments for
204 both the DSI and MSI samples (Fig.7 A,B). Qualitative comparison of these maps shows
205 a reliable and highly similar pattern of segmentation between the two pallidal regions.
206 This is particularly evident in regions where outer and inner segments are divided along
207 a curve approximately situated on the internal medullary lamina in both hemispheres
208 (Fig.7 A,B, and coronal slices Fig.7 D-E).

209

210 While these segmentation maps are not as clean as the hand-drawn maps based on the
211 T1 signal (Fig. 2A), the general pattern of clustering is much better than expectations
212 from chance. To explicitly quantify this, we compared the automatic segmentations to
213 the hand drawn maps against chance accuracies generated from a permutation test
214 (see Methods). Random accuracies ranged from 22% to 77% and were consistently
215 higher in the inner segment (37% to 77%) relative to the outer segment (22% to 62%)
216 reflecting the fact that there were fewer voxels within the inner segment and thus a
217 higher chance of randomly overlapping with the correct assignment. As can be seen in
218 Fig. 8, our classification significantly outperformed chance in all cases except the right
219 hemisphere of the outer segment in the MSI dataset (Fig. 8C). Furthermore, accuracies
220 were generally higher in the DSI sample than the MSI sample, likely due to the fact that
221 the DSI sample was separable along all three features included in the clustering, while
222 the MSI sample was not clearly separable based on the sensitivity curve measure (Fig.
223 6G-H).

224

225 Consistency across data sets

226 So far we have shown that both DSI and MSI samples exhibit similar differences in the
227 pallidal segment diffusion signals and similar automatic parcellations of the internal and
228 external pallidal masks. In order to quantify the similarity of the results between the two
229 samples, we correlated the voxelwise probabilities between the DSI and MSI datasets
230 (Fig. 9) for the internal and external segments separately. Overall, voxelwise
231 probabilities between the two samples were moderately correlated in both hemispheres
232 ($r(138) = 0.67$ in left hemisphere vs. $r(138) = 0.56$ in the right hemisphere), suggesting
233 that the SDF signal is capturing reliable topographic differences in underlying
234 microstructural properties that is generally consistent across samples and the type of
235 diffusion imaging approach used.

236

237 Because both the DSI and MSI samples provided similar probability profiles, we
238 aggregated both data sets to form a composite probabilistic map of the internal and
239 external pallidal segments based on the underlying diffusion structure. These merged
240 maps are shown in Figure 7C,F. Collapsing across the two acquisition methods
241 revealed an even clearer distinction between the two pallidal nuclei. This confirms that
242 classification-based purely on the properties of the diffusion signal is sufficiently robust
243 across differences in acquisition approach and scan environments to capture the major
244 divisions of the inner and outer segments of the globus pallidus.

245

246 **Discussion**

247 For the first time we are able to show that the orientation distribution of the diffusion
248 within the human pallidum is consistent with the presence of nigral and striatal efferents
249 that run through these nuclei. Because a large portion of these pathways is buried within
250 the pallidum, a region of high iron density, visualization of these efferents has been
251 challenging with conventional imaging approaches. If diffusion MRI proves to be a
252 reliable method of assessing the integrity of these pathways and their degradation in
253 movement disorders, then quantifying degradation within the pallidum will be necessary
254 to obtain accurate measurements of associated changes. Here we show that the SDF
255 was also able to pick up on established histological differences between the internal and
256 external segment of the globus pallidus (Hardman et al., 2002, Eid et al., 2013, Difiglia
257 and Rafols 1988), resulting in the first automatic segmentation of these two nuclei.
258 Thus, these measures are sufficiently robust to detect known differences in the pallidal
259 segments. Furthermore, these differences in the diffusion signal between the internal
260 and external segments were mostly consistent regardless of the acquisition method
261 used (i.e., DSI vs. MSI) and able to classify the separate segments with accuracies well
262 above chance expectations.

263

264 Although diffusion anisotropy measures are typically used to visualize pathways within
265 core white matter regions of the brain, here we showed that tissue characteristics
266 derived from the diffusion MRI signal, including differences in connectivity, intensity and
267 sensitivity, can distinguish nuclear properties within the pallidum itself (see also Wiegell
268 et al., 2003; Mang et al., 2012). We presume that orientations of the fibers in the two

269 pallidal nuclei along with differences in density and myelination contribute to the
270 characteristics of the SDFs within these voxels (Beaulieu, 2002). The predominately
271 dorsolateral orientation of the resolved fiber peaks within the pallidal segments is
272 consistent with the primary orientation of the striatopallidal, striatonigral and
273 nigrostriatal/pallidal tracts (Wilson 1914, Szabo 1967, Szabo 1962, Fox and Rafols,
274 1976, Carpenter and Peter, 1972). The more pronounced dorsolateral orientation of the
275 internal segment compared to the external segment in both the primary (Fig. 3) and
276 secondary fibers (Fig. 4) is consistent with the volumetric differences between the two
277 segments, since the nigrostriatal and striatonigral fibers traverse both segments. The
278 medial shift observed in the outer segment (Fig. 3) is likely reflecting a distinct fiber
279 system, possibly projections from the subthalamic nucleus. This open question can be
280 resolved by a direct comparison of SDFs with postmortem histological analysis, which
281 should be a goal of future work.

282

283 We should point out that the orientation of the peak fibers may not be completely
284 consistent across diffusion imaging approaches. For example, there is a more
285 pronounced medial shift in the external segment orientations in the DSI sample (Fig.3
286 A,B) than in the MSI sample (Fig.3 C,D). This may be due to the fact that the DSI
287 sample is more sensitive to underlying microarchitectural features that contribute to a
288 medial bias in the SDF signal. However, the secondary fiber in this sample was oriented
289 in a more dorsal and dorsolateral direction (Fig. 4). This suggests that these nigral and
290 striatal efferents are also present in the DSI sample, but to a weaker degree than in the

291 MSI sample. This difference is likely due to the diffusion sampling scheme used in DSI
292 and MSI. The DSI used a stronger diffusion sensitization strength (i.e. higher b-value)
293 than the MSI, and it is more sensitive to restricted diffusion in gray matter.

294

295 Being able to detect signatures of the underlying cellular content of the pallidal nuclei *in*
296 *vivo* has enormous potential as a biomarker for the integrity of basal ganglia pathways
297 and their pathology. Many movement disorders involve degradation of specific pathways
298 within the GPe and the GPi. In Parkinson's disease for example, dopaminergic neurons
299 within the substantia nigra degenerate which leads to a loss of the nigrostriatal fibers.

300 Degradation of the nigrostriatal efferents in Parkinson's patients have been recently
301 identified using diffusion MRI (Ziegler et al., 2014). Given that the nigrostriatal fibers
302 travel through the pallidum, degradation of these pathways may be reflected in the
303 integrity of the microstructural architecture exhibited by the SDFs within the pallidum.

304 Future comparative and clinical studies are needed in order to validate this assumption.

305

306 Beyond clinical implications, our results also have relevance to the investigation of basal
307 ganglia function in neurologically healthy individuals. In the canonical direct-indirect
308 pathway model of motor facilitation (Albin et al., 1989, DeLong 2000), activity in the GPe
309 is correlated with inhibiting movement initiation, through disinhibition of the sub-thalamic
310 nucleus, which in turn excites the GPi/SNr. Conversely, during movement facilitation,
311 activity within the GPi decreases. Dysfunction of the direct and indirect pathways results
312 in an imbalance between the two circuits, which causes impaired motor production as

313 seen in Parkinson's and Huntington's disease. If the efficiency of processing with
314 striatopallidal pathways is reflected in their microstructural integrity, then individual
315 variation in performance on tasks may be correlated with the QA distributions of the
316 striatopallidal fiber systems.

317

318 While our present results show promise for using the diffusion imaging signal as a
319 measure of cellular architecture within sub-cortical nuclei, this approach still has some
320 inherent limitations. First, as mentioned previously, diffusion imaging provides an
321 indirect measure of cellular architecture. While validation work in non-human animals
322 has provided insights into the underlying cellular properties for white matter using
323 tensor-based reconstruction approaches (Wang et al., 2011, Wang et al., 2014, Thomas
324 et al., 2014), model-based approaches have not been validated against histological
325 models, particularly in gray matter (Blumenfeld-Katzir et al., 2011). Therefore, we do
326 not know for sure what properties of the SDF reflect what properties of the underlying
327 tissue. Future studies could probe precisely how changes in SDF properties are
328 associated with variations in density, number of fibers, and myelination, by combining
329 histological analysis and diffusion imaging in animal models and post mortem tissue
330 analysis of the pallidum.

331

332 In addition, although we demonstrated that the boundaries of the pallidal nuclei are
333 resolvable based solely on diffusion information, the segmentations are imperfect. In
334 particular, there is a cluster of voxels in the anterior region of the pallidum that was

335 misclassified in a significant number of subjects, and the parcellations were less
336 accurate in the MSI data set as a whole. The proximity of the globus pallidus to the
337 major white matter tracts of the internal capsule may contribute to partial voluming
338 problems that contaminate the SDF signal in these voxels, resulting in classification
339 errors. Future work could adaptively cluster using more sophisticated approaches to
340 allow for noise clusters that could arise from errors in masking.

341

342 Despite this partial voluming problem, the segmentation results reported here still
343 provide evidence of robust differences between the segments of the human pallidum.
344 For example, unlike most subcortical parcellations (e.g. Behrens et al., 2003), we are
345 not supplementing the clustering features with additional distance information that adds
346 a strong prior on expected location of the nuclei. Such spatial priors would dramatically
347 clean up the underlying maps; however, the distance from the expected nuclear location
348 would become the dominant clustering feature. Although omitting these priors may lead
349 to noisier segmentations, our approach provides a more robust measure for future
350 studies to assess the pallidal cellular integrity in clinical populations.

351

352 Regardless of these limitations we have shown that the inner and outer segments of the
353 globus pallidus not only express common asymmetries in their underlying SDFs,
354 consistent with major efferent pathways, but also reliably differ among several
355 properties of the diffusion signals. This was reliable enough that a simple and automatic
356 clustering approach, based on properties of the SDF, resolved the inner and outer

357 segments better than chance, regardless of the imaging acquisition used (i.e., DSI or
358 MSI). This population atlas based analysis approach enables future studies to quantify
359 the extent to which microstructural variability correlates with functional properties of the
360 system, such as individual differences in inhibitory control ability and or clinical
361 pathologies of the underlying fiber systems, providing a powerful new tool for
362 investigating the cellular architecture of basal ganglia systems in vivo.

363

364 **Materials and Methods**

365 *Participants and Acquisition*

366 Two separate types of diffusion imaging were used for our analysis.

367

368 Diffusion Spectrum Imaging (DSI: CMU-60 Dataset): Twenty nine male and thirty
369 one female subjects were recruited from the local Pittsburgh community and the
370 Army Research Laboratory in Aberdeen Maryland. All subjects were
371 neurologically healthy, with no history of either head trauma or neurological or
372 psychiatric illness. Subject ages ranged from 18 to 45 years of age at the time of
373 scanning, with a mean age of 26 years (+/- 6 standard deviation). Six subjects
374 were left handed (3 males, 3 females).

375 All participants were scanned on a Siemen's Verio 3T system in the
376 Scientific Imaging & Brain Research (SIBR) Center at Carnegie Mellon University
377 using a 32-channel head coil. We collected a 50 min, 257-direction DSI scan
378 using a twice-refocused spin-echo EPI sequence and multiple q values (TR =

379 9,916 ms, TE = 157 ms, voxel size = 2.4mm³, FoV = 231 x 231 mm, b-max =
380 5,000 s/mm², 51 slices). Head-movement was minimized during the image
381 acquisition through padding supports and all subjects were confirmed to have
382 minimal head movement during the scan prior to inclusion in the template.

383

384 Multi-shell Imaging (MSI; HCP-80 Dataset): The data were from the Human
385 connectome project at WashU-Minnesota Consortium (Q1 release). Thirty six
386 male and forty two female subjects were scanned on a customized Siemens 3T
387 “Connectome Skyra” housed at Washington University in St. Louis. Subject ages
388 ranged from 22-36 years of age at the time of scanning, with a mean age of
389 29.44 (+/- 3.5 standard deviation). All subjects were healthy, with no history of
390 neurological or psychiatric illness. The two subjects that have subsequently been
391 found by the HCP to exhibit gray matter heterotopia have been excluded from
392 this analysis. The HCP DWI session was acquired using a spin-echo EPI
393 sequence and (TR = 5520 ms, TE = 89.5 ms, voxel size = 1.25 mm³, FoV = 210
394 x 180, 3 shells of b = 1000, 2000, 3000 s/mm², 111 slices, 90-directions for each
395 shell).

396

397 *Diffusion MRI Reconstruction*

398 All images were processed with a q-space diffeomorphic reconstruction method
399 described previously (Yeh and Tseng, 2011) using DSI Studio ([http://dsi-](http://dsi-studio.labsolver.org/)
400 [studio.labsolver.org/](http://dsi-studio.labsolver.org/)). The SDFs were reconstructed to a spatial resolution of 1 mm³.

401 The white matter surface is rendered independently from an externally supplied 1 mm³
402 resolution white matter template. The quantitative anisotropy (QA; Yeh et al., 2010) and
403 fiber orientation of the two major fibers in each voxel were exported into a separate file
404 for analysis.

405

406 *SDF Analysis*

407 Masks of the inner and outer segments of the pallidum were manually drawn by
408 identifying the internal medullary lamina in each hemisphere on the high resolution T1
409 ICBN MNI template. In each hemisphere, the GPe was drawn by including those voxels
410 between the anterior and posterior limbs of the internal capsule, the putamen, and the
411 internal medullary lamina (outer left/right in Fig.2A). Similarly, the GPi was drawn by
412 including the voxels between the internal medullary lamina, the posterior limb and genu
413 of the internal capsule (inner left/right in Fig.2A). All region of interest masks were drawn
414 in MRICron (Rorden and Brett, 2000) and exported as NifTI images.

415

416 We then isolated the SDFs within each voxel of both region masks for analysis. For
417 illustration, Fig. 2B shows a schematized version of a SDF illustrating three resolved
418 fibers, with their independent magnitude (i.e., lengths, reflecting QA) and orientation.
419 Two representative 3D SDFs from a voxel within the left GPi and a voxel within the left
420 GPe are shown in Fig. 2 C,D. For each voxel, we took three independent measures of
421 the SDF structure: the principal fiber orientation, the number of resolved fibers across a
422 range of QA thresholds, and QA magnitude of the principal fiber. To generate the

423 angular distribution histograms (Figs. 3,4), we used the circstat toolbox (Berens 2009)
424 and computed the circular mean of the voxel orientations across subjects. The internal
425 capsule orientation (green arrows in Fig. 3,4) was calculated by averaging the
426 orientations across a 4mm^3 voxel cube situated prominently within the internal capsule
427 in the left and right hemispheres. For plotting purposes, a gaussian smoothing kernel
428 was applied to the QA maps (Fig. 6 A-D) for each subject (2 FWHM).

429

430 We extracted the primary fiber orientation, the number of fibers in each voxel, and the
431 QA of the primary fiber from all voxels in each mask. Then we clustered the combined
432 data across both masks using these diffusion features with a standard clustering
433 approach in Matlab (R2014a). We specified two clusters, used squared euclidean
434 distance as the distance metric and the k-means++ algorithm for cluster center
435 initialization (replicates = 10). The clusters to the inner and outer segment were
436 assigned based on the number of correctly assigned voxels relative to the hand drawn
437 masks. This algorithm generated inner and outer segment maps for each subject and
438 hemisphere in each dataset. To generate the probabilistic maps of each segment
439 across all subjects in a sample (Fig. 7), voxel probabilities were estimated by averaging
440 the binary categorization of each voxel in the inner and outer segment maps. Separate
441 probability masks were calculated for in the DSI and MSI data sets, as well as across
442 both samples (Merged). In order to quantify accuracy, we defined the classification
443 accuracy as the number of voxels correctly assigned to the inner/outer segment from

444 the k-means analysis using the manual segmentation as the correct assignment divided
445 by the total number of voxels in that segment (Fig. 8).

446

447 Accuracy of the clustered segments was compared against the hand-segmented region
448 of interest masks and a chance null distribution was estimated using a permutation
449 procedure. On each iteration of the permutation test, every pallidal voxel was
450 pseudorandomly assigned to either the inner or outer segment. The voxel's permuted
451 assignment was then compared to the voxel's real assignment in the manually
452 segmented pallidum masks and counted as correct if it matched that assignment. All of
453 the correct assignments were counted for each iteration of the permutation test
454 (n=1000). Chance accuracies were tallied across all iterations and the number of
455 instances that the random assignment performed better than k-means classification was
456 divided by the total number of iterations to generate the p-value for how well the
457 automated classification performs against a classification based purely on chance.

458

459 Acknowledgements

460 Data were provided [in part] by the Human Connectome Project, WU-Minn Consortium
461 (Principal Investigators: David Van Essen and Kamil Ugurbil; 1U54MH091657) funded
462 by the 16 NIH Institutes and Centers that support the NIH Blueprint for Neuroscience
463 Research; and by the McDonnell Center for Systems Neuroscience at Washington
464 University. This project was also supported by the Army Research Laboratory under
465 Cooperative Agreement Number W911NF-10-2-0022. The views and conclusions

466 contained in this document are those of the authors and should not be interpreted as
467 representing the official policies, either expressed or implied, of the Army Research
468 Laboratory or the U.S. Government. The U.S. Government is authorized to reproduce
469 and distribute reprints for Government purposes notwithstanding any copyright notation
470 herein. This research was also supported in part by T32 NS007433-17.

471

References

- 472 Abhinav, K., Yeh, F.-C., Pathak, S., Friedlander, R. M., & Fernandez-Miranda, J. C.
473 (2014). Advanced diffusion MRI fiber tracking in neurosurgical and
474 neurodegenerative disorders and neuroanatomical studies: A review. *Biochimica et*
475 *Biophysica Acta (BBA) - Molecular Basis of Disease*.
476 doi:10.1016/j.bbadis.2014.08.002
- 477 Albin, R. L., Young, A. B., & Penney, J. B. (1989). The functional anatomy of basal
478 ganglia disorders. *Trends in Neurosciences*, 12(10), 366–375. doi:10.1016/0166-
479 2236(89)90074-X
- 480 Alexander, G. E., DeLong, M. R., & Strick, P. L. (1986). Parallel organization of
481 functionally segregated circuits linking basal ganglia and cortex. *Annual Review of*
482 *Neuroscience*, 9, 357–381. doi:10.1146/annurev.neuro.9.1.357
- 483 Amunts, K., Lepage, C., Borgeat, L., Mohlberg, H., Dickscheid, T., Rousseau, M.-É., ...
484 Evans, A. C. (2013). BigBrain: an ultrahigh-resolution 3D human brain model.
485 *Science (New York, N.Y.)*, 340(6139), 1472–5. doi:10.1126/science.1235381
- 486 Bastiani, M., Shah, N. J., Goebel, R., & Roebroeck, A. (2012). Human cortical
487 connectome reconstruction from diffusion weighted MRI: The effect of tractography
488 algorithm. *NeuroImage*, 62(3), 1732–1749. doi:10.1016/j.neuroimage.2012.06.002
- 489 Behrens, T. E. J., Johansen-Berg, H., Woolrich, M. W., Smith, S. M., Wheeler-
490 Kingshott, C. A. M., Boulby, P. A., ... Matthews, P. M. (2003). Non-invasive
491 mapping of connections between human thalamus and cortex using diffusion
492 imaging. *Nature Neuroscience*, 6(7), 750–757.
493 doi:10.1227/01.NEU.0000309595.77090.89
- 494 Beaulieu, C. (2002). The basis of anisotropic water diffusion in the nervous system - A
495 technical review. *NMR in Biomedicine*. doi:10.1002/nbm.782
- 496 Berens, P. (2009). CircStat: A MATLAB toolbox for circular statistics. *Journal of*
497 *Statistical Software*, 31, 1–21. doi:10.1002/wics.10
- 498 Beaulieu C. The basis of anisotropic water diffusion in the nervous
499 syste. *NMR Biomed*. 2002; 15: 435–455
- 500 Blumenfeld-Katzir, T., Pasternak, O., Dagan, M., & Assaf, Y. (2011). Diffusion MRI of
501 structural brain plasticity induced by a learning and memory task. *PLoS ONE*, 6(6).
502 doi:10.1371/journal.pone.0020678
- 503 Burke, R. E., & O'Malley, K. (2013). Axon degeneration in Parkinson's disease.
504 *Experimental Neurology*. doi:10.1016/j.expneurol.2012.01.011

505

- 506 Carpenter, M. B., & Peter, P. (1972). Nigrostriatal and nigrothalamic fibers in the rhesus
507 monkey. *The Journal of Comparative Neurology*, 144(1), 93–115.
508 doi:10.1002/cne.901440105
- 509 Carpenter, M. B., & McMasters, R. E. (1964). Lesions of the Substantia Nigra in the
510 Rhesus Monkey. Efferent Fiber Degeneration and Behavioral Observations. *The*
511 *American Journal of Anatomy*, 114, 293–319.
- 512 Cossette, M., Lévesque, M., & Parent, A. (1999). Extrastriatal dopaminergic innervation
513 of human basal ganglia. *Neuroscience Research*, 34(1), 51–54.
- 514 DeLong, M. R. (1990). Primate models of movement disorders of basal ganglia origin.
515 *Trends in Neurosciences*, 13(7), 281–285. doi:10.1016/0166-2236(90)90110-V
- 516 Difiglia, M., & Rafols, J. A. (1988). Synaptic organization of the globus pallidus. *Journal*
517 *of Electron Microscopy Technique*, 10(3), 247–263. doi:10.1002/jemt.1060100304
- 518 Eid, L., Champigny, M. F., Parent, A., & Parent, M. (2013). Quantitative and
519 ultrastructural study of serotonin innervation of the globus pallidus in squirrel
520 monkeys. *European Journal of Neuroscience*, 37(10), 1659–1668.
521 doi:10.1111/ejn.12164
- 522 Fernández-Miranda, J. C., Wang, Y., Pathak, S., Stefaneau, L., Verstynen, T., & Yeh, F.
523 C. (2014). Asymmetry, connectivity, and segmentation of the arcuate fascicle in the
524 human brain. *Brain Structure and Function*. doi:10.1007/s00429-014-0751-7
- 525 Fox, C. A., & Rafols, J. A. (1976). The striatal efferents in the globus pallidus and in the
526 substantia nigra. *Research Publications - Association for Research in Nervous and*
527 *Mental Disease*, 55, 37–55.
- 528 Haber, S. N., Fudge, J. L., & McFarland, N. R. (2000). Striatonigrostriatal pathways in
529 primates form an ascending spiral from the shell to the dorsolateral striatum. *The*
530 *Journal of Neuroscience : The Official Journal of the Society for Neuroscience*,
531 20(6), 2369–2382. doi:http://www.jneurosci.org/content/20/6/2369
- 532 Haber, S. N. (2003). The primate basal ganglia: Parallel and integrative networks. In
533 *Journal of Chemical Neuroanatomy* (Vol. 26, pp. 317–330).
534 doi:10.1016/j.jchemneu.2003.10.003
- 535 Hardman, C. D., Henderson, J. M., Finkelstein, D. I., Horne, M. K., Paxinos, G., &
536 Halliday, G. M. (2002). Comparison of the basal ganglia in rats, marmosets,
537 macaques, baboons, and humans: Volume and neuronal number for the output,
538 internal relay, and striatal modulating nuclei. *Journal of Comparative Neurology*,
539 445(3), 238–255. doi:10.1002/cne.10165

- 540 Hollerman, J. R., Tremblay, L., & Schultz, W. (2000). Involvement of basal ganglia and
541 orbitofrontal cortex in goal-directed behavior. In *Progress in Brain Research* (Vol.
542 126, pp. 193–215). doi:10.1016/S0079-6123(00)26015-9
- 543 Mang, S. C., Busza, A., Reiterer, S., Grodd, W., & Klose, A. U. (2012). Thalamus
544 segmentation based on the local diffusion direction: A group study. *Magnetic
545 Resonance in Medicine*, 67(1), 118–126. doi:10.1002/mrm.22996
- 546 Reiner, A., Albin, R. L., Anderson, K. D., D'Amato, C. J., Penney, J. B., & Young, A. B.
547 (1988). Differential loss of striatal projection neurons in Huntington disease.
548 *Proceedings of the National Academy of Sciences of the United States of America*,
549 85(15), 5733–5737. doi:10.1073/pnas.85.15.5733
- 550 Rorden, C., & Brett, M. (2000). Stereotaxic display of brain lesions. *Behavioural
551 Neurology*, 12(4), 191–200.
- 552 Szabo, J. (1967). The efferent projections of the putamen in the monkey. *Experimental
553 Neurology*, 19(4), 463–476. doi:10.1016/0014-4886(67)90166-5
- 554 Szabo, J. (1962). Topical distribution of the striatal efferents in the monkey.
555 *Experimental Neurology*, 5(1), 21–36. doi:10.1016/0014-4886(62)90067-5
- 556 Thomas, C., Ye, F. Q., Irfanoglu, M. O., Modi, P., Saleem, K. S., Leopold, D. A., &
557 Pierpaoli, C. (2014). Anatomical accuracy of brain connections derived from
558 diffusion MRI tractography is inherently limited. *Proceedings of the National
559 Academy of Sciences*, 111(46), 16574–16579. doi:10.1073/pnas.1405672111
- 560 Wang, Y., Fernández-Miranda, J. C., Verstynen, T., Pathak, S., Schneider, W., & Yeh,
561 F. C. (2013). Rethinking the role of the middle longitudinal fascicle in language and
562 auditory pathways. *Cerebral Cortex*, 23(10), 2347–2356.
563 doi:10.1093/cercor/bhs225
- 564 Wang, Y., Wang, Q., Haldar, J. P., Yeh, F. C., Xie, M., Sun, P., ... Song, S. K. (2011).
565 Quantification of increased cellularity during inflammatory demyelination. In *Brain*
566 (Vol. 134, pp. 3587–3598). doi:10.1093/brain/awr307
- 567 Wang, X., Cusick, M. F., Wang, Y., Sun, P., Libbey, J. E., Trinkaus, K., ... Song, S. K.
568 (2014). Diffusion basis spectrum imaging detects and distinguishes coexisting
569 subclinical inflammation, demyelination and axonal injury in experimental
570 autoimmune encephalomyelitis mice. *NMR in Biomedicine*, 27(7), 843–852.
571 doi:10.1002/nbm.3129
- 572 Wedeen, V. J., Wang, R. P., Schmahmann, J. D., Benner, T., Tseng, W. Y. I., Dai, G.,
573 ... de Crespigny, A. J. (2008). Diffusion spectrum magnetic resonance imaging
574 (DSI) tractography of crossing fibers. *NeuroImage*, 41(4), 1267–1277.
575 doi:10.1016/j.neuroimage.2008.03.036

- 576 Wiegell, M. R., Tuch, D. S., Larsson, H. B., & Wedeen, V. J. (2003). Automatic
577 segmentation of thalamic nuclei from diffusion tensor magnetic resonance imaging.
578 *Neuroimage*, 19(2 Pt 1), 391–401. doi:10.1016/S1053-8119(03)00044-2
- 579 Wilson, S. a K. (1914). An experimental research into the anatomy and physiology of
580 the corpus striatum. *Brain*, 36, 427–492.
- 581 Yeh, F. C., & Tseng, W. Y. I. (2011). NTU-90: A high angular resolution brain atlas
582 constructed by q-space diffeomorphic reconstruction. *NeuroImage*, 58(1), 91–99.
583 doi:10.1016/j.neuroimage.2011.06.021
- 584 Yeh, F. C., Wedeen, V. J., & Tseng, W. Y. I. (2010). Generalized q-sampling imaging.
585 *IEEE Transactions on Medical Imaging*, 29(9), 1626–1635.
586 doi:10.1109/TMI.2010.2045126
- 587 Ziegler, E., Rouillard, M., André, E., Coolen, T., Stender, J., Balteau, E., ... Garraux, G.
588 (2014). Mapping track density changes in nigrostriatal and extranigral pathways in
589 Parkinson's disease. *NeuroImage*, 99, 498–508.
590 doi:10.1016/j.neuroimage.2014.06.033

591
592
593

594

595

596

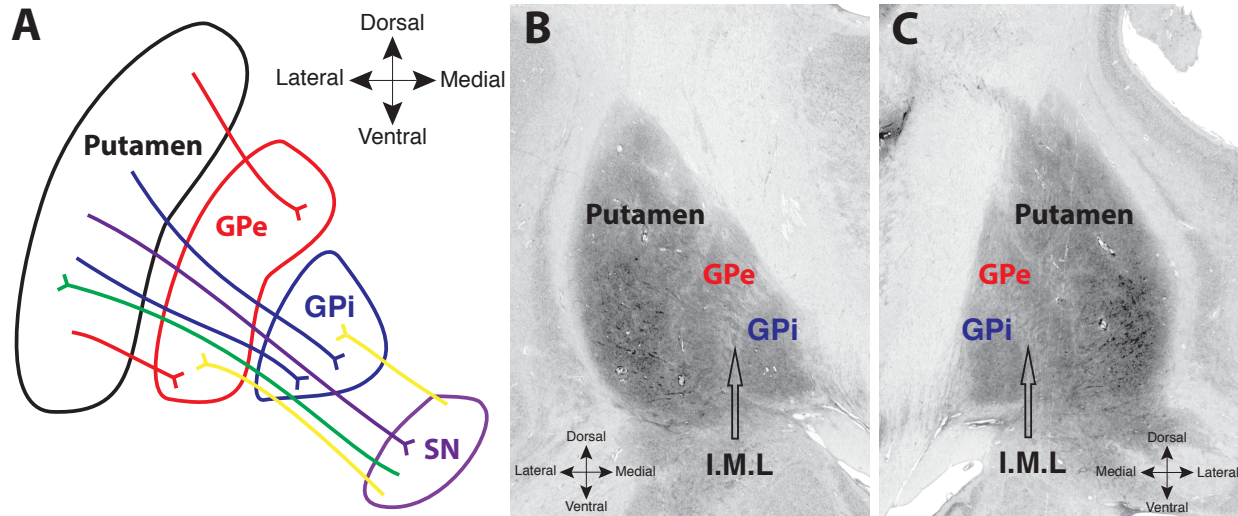
597

598

599

600

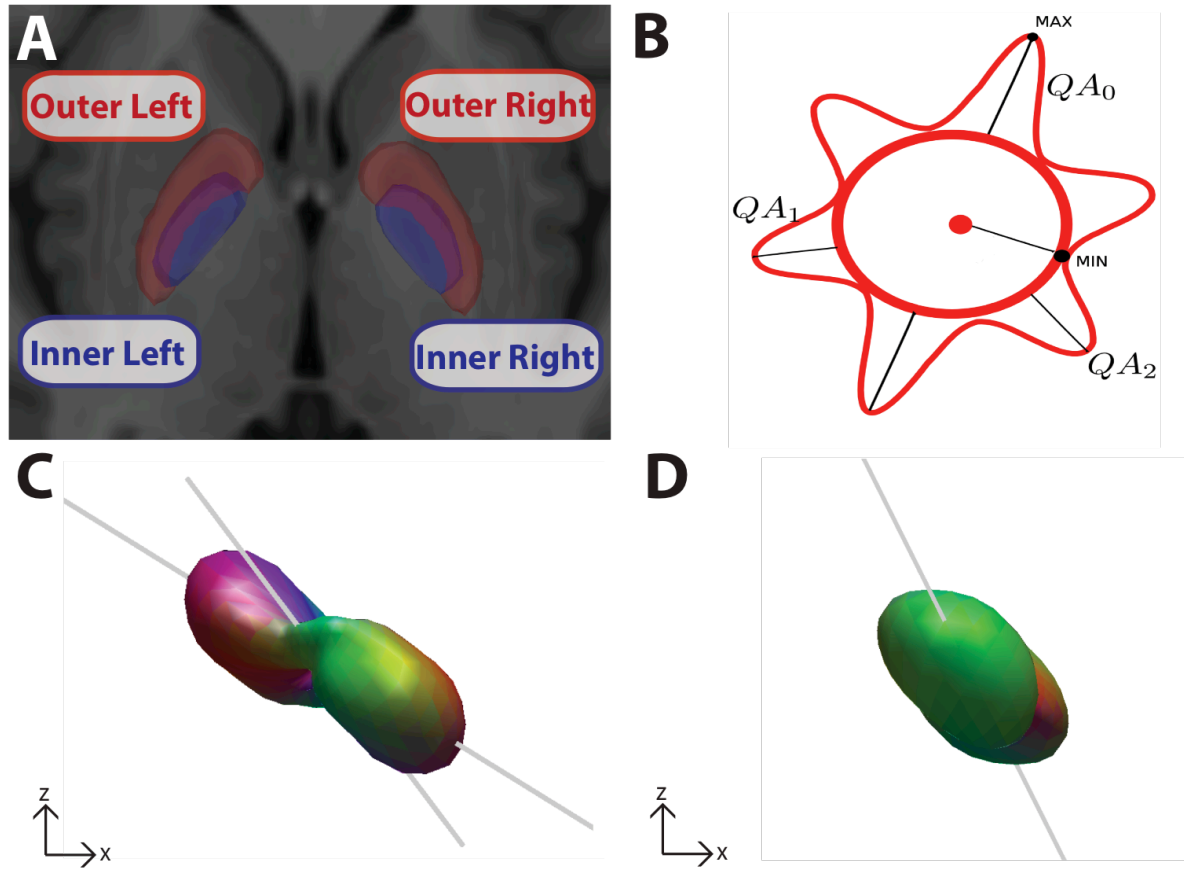
601



602

603 Fig. 1

604 A. Schematic of fiber systems traversing the internal (GPi) and external (GPe) segments
605 of the pallidum, including projections to and from the substantia nigra. Labeled
606 pathways include nigrostriatal (green) striatopallidal (red, cyan), striatolnigral (purple)
607 and nigropallidal (yellow (red, blue), striatonigral (purple) and nigropallidal (yellow). B
608 and C. Coronal images from the Big Brain atlas, showing the putamen, GPe, and GPi, in
609 the left (B) and right (C) hemispheres; black arrows point to the approximate center of
610 the internal medullary lamina (I.M.L.) separating the two segments (slice 3894, Amunts
611 2013).

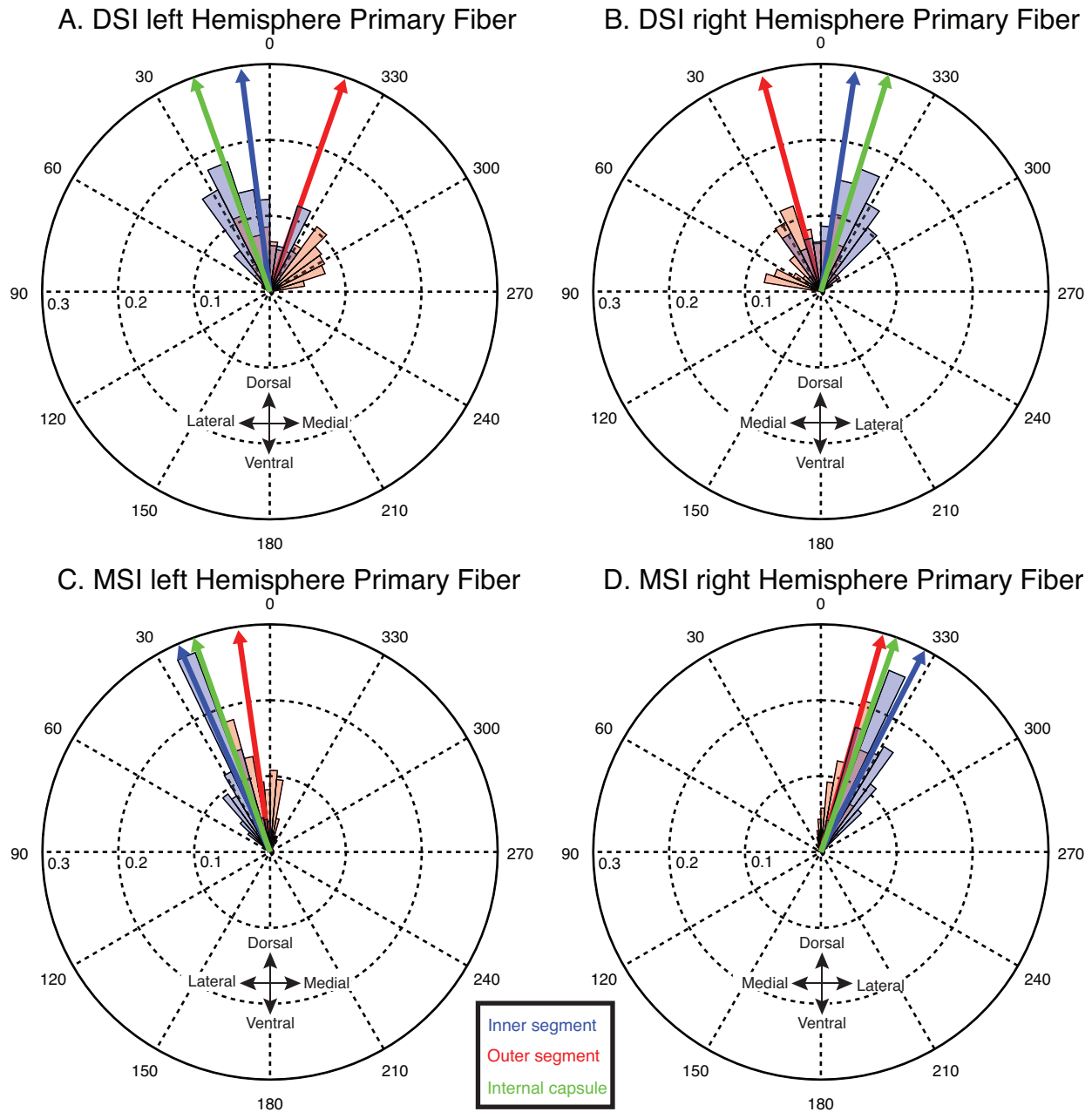


612

613 Fig. 2

614 A. The inner (blue) and outer (red) segments of the left and right pallidum were
615 manually drawn on the high resolution T1 ICBM 152 template. B. Schematized version
616 of an SDF illustrating three resolved fibers (QA0, QA1, QA2), their magnitude (i.e.,
617 lengths, reflecting QA) and orientation. C,D Representative SDFs from the left internal
618 segment (C) and left external segment (D) in the coronal plane from a single subject
619 from the DSI dataset. Gray lines indicate direction of fiber orientations.

Primary Fiber



620

621

622

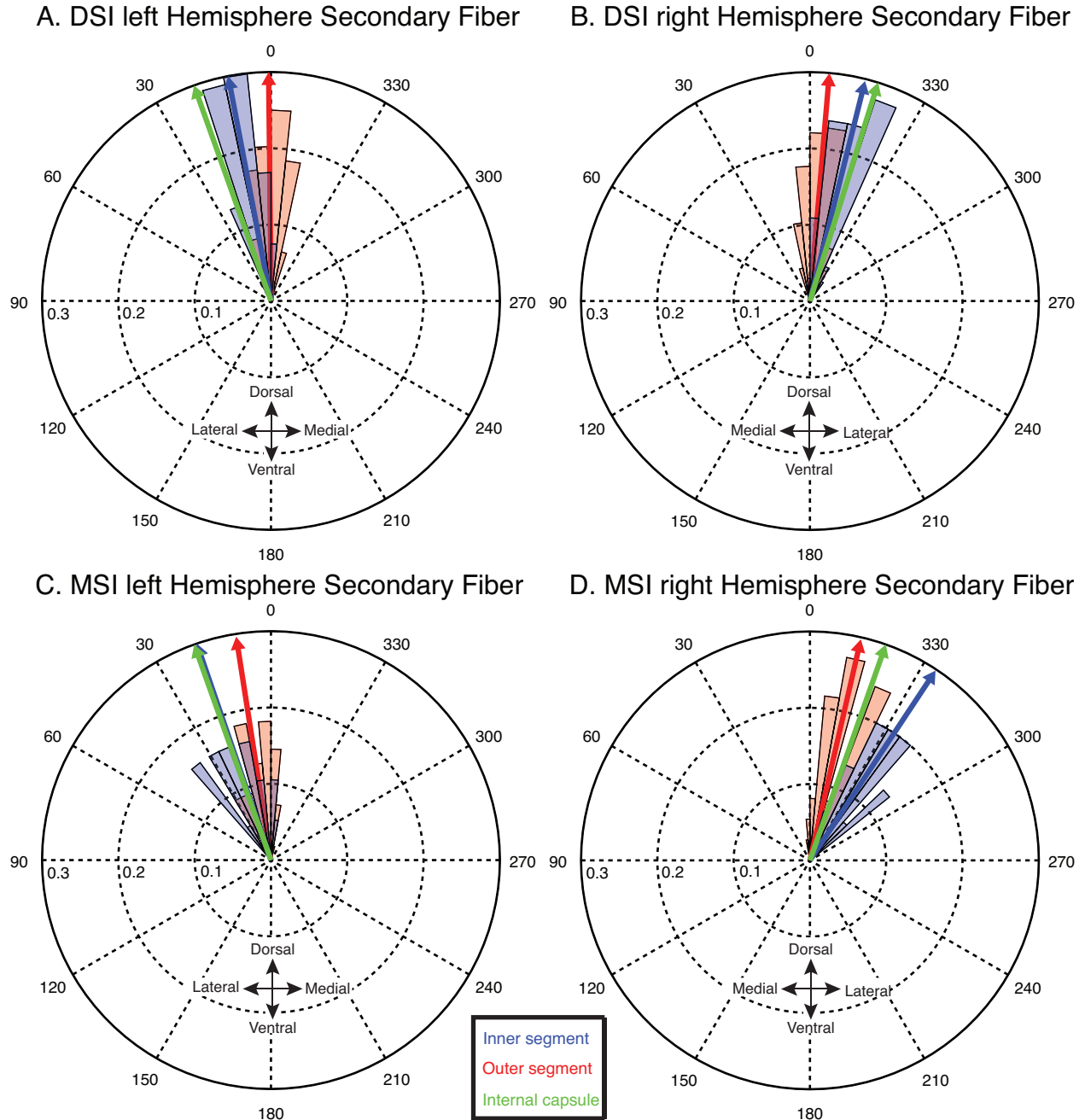
623

624

625

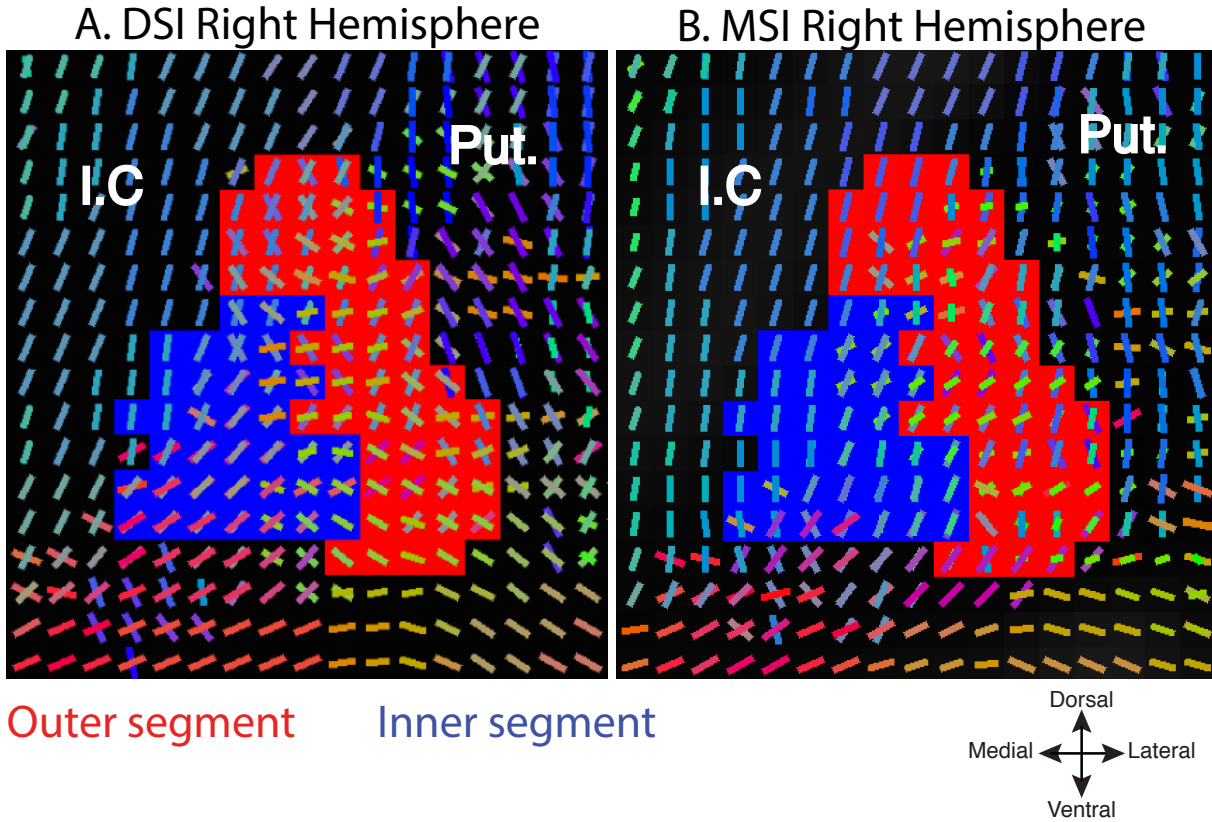
Fig. 3
Angular distributions of primary fibers from DSI (A,C) and MSI (C,D) datasets. Blue, red, and green arrows indicate the mean of the distributions in the inner, outer and internal capsule respectively.

Secondary Fiber

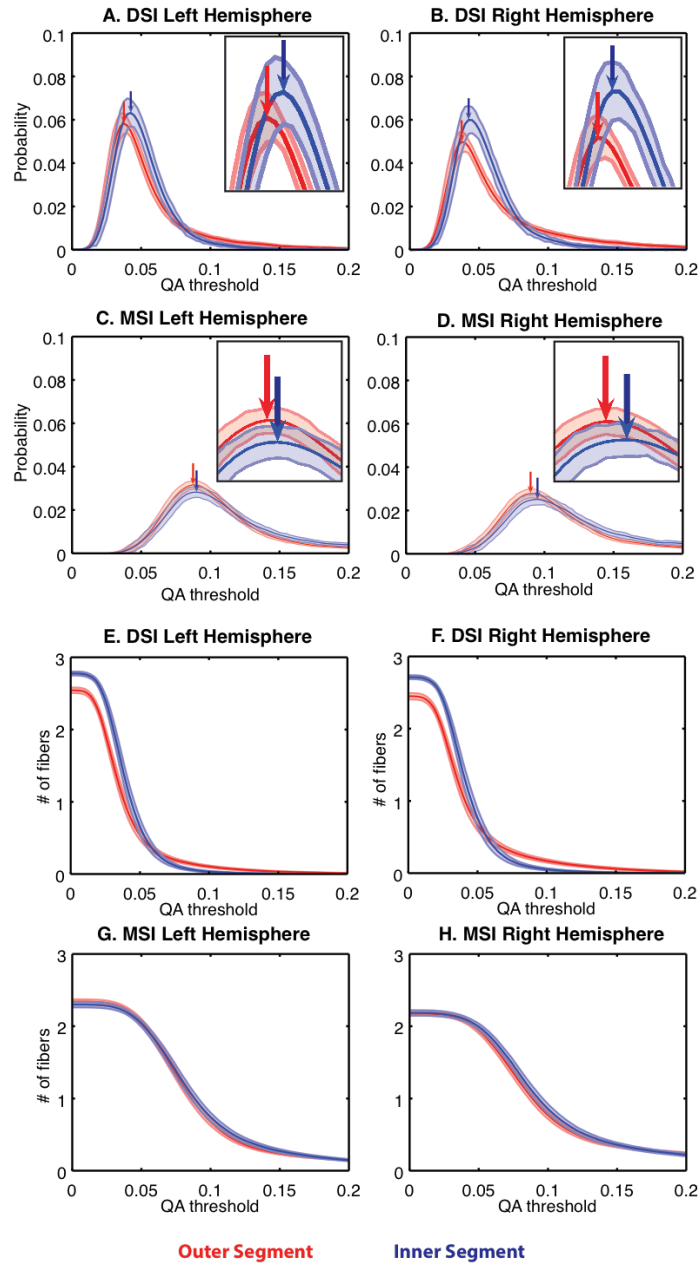


626
627
628
629
630

Fig. 4
Angular distributions of secondary fibers from DSI (A,C) and MSI (C,D) datasets. Blue, red, and green arrows indicate the mean of the distributions in the inner, outer and internal capsule respectively.



631
632 Fig. 5
633 Voxelwise geometries of the primary and secondary fibers, inner (blue) and outer (red),
634 segments of two example subjects from the DSI (A) and MSI (B) datasets. Slices are
635 both from $y = -1$ (MNI). (Putamen (Put.), Internal capsule (I.C.)). Fiber orientations are
636 color coded according to their orientation.



637

638

639 Fig. 6

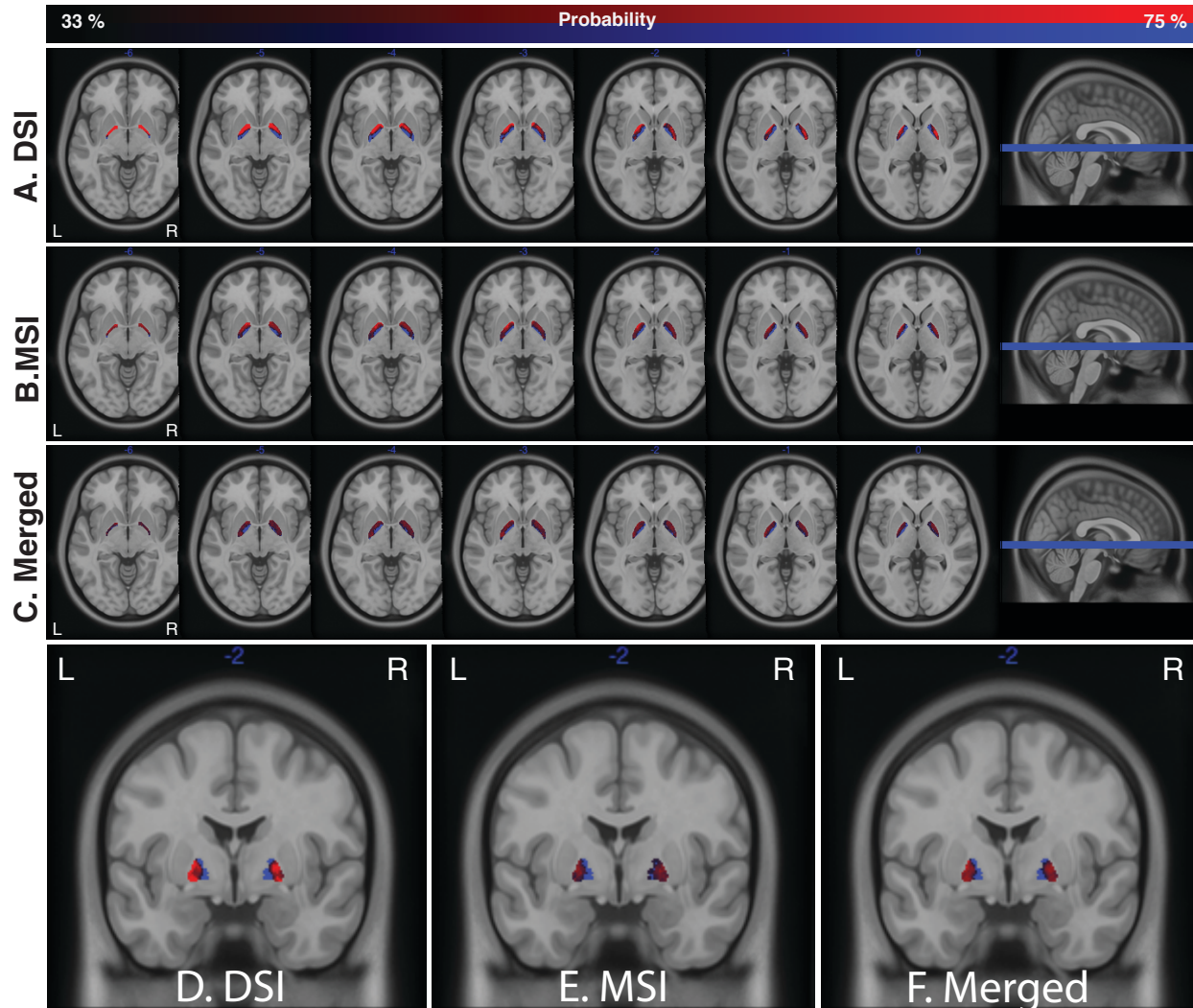
640 A-D. Probability density functions of the primary fiber QA of the inner (blue) and outer

641 (red) segments in the DSI(A,B) and MSI(C,D) datasets. E-H The number of resolved

642 fibers thresholded by QA in the inner and outer segments in the DSI (A,B) and MSI

643 datasets (C,D). Arrows indicate peaks of the distributions. Lines indicate mean and

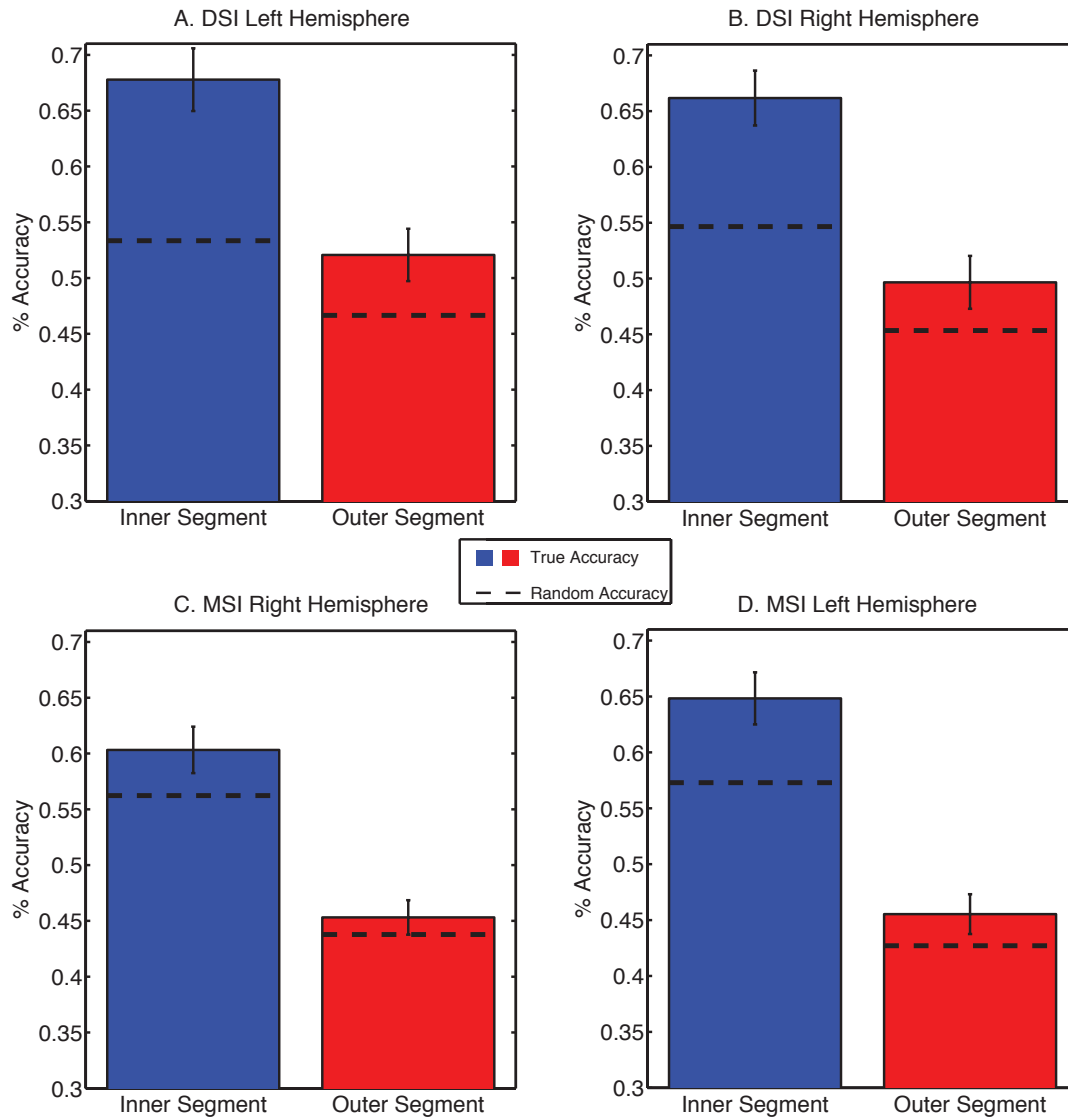
644 shaded regions are 95% confidence intervals.



645
646
647
648
649
650
651
652

Fig. 7

A-C. Probabilistic maps, across subjects, of the inner and outer segments in the DSI (A), MSI (B), and merged (C) datasets. Maps are thresholded between 33-77% probability. The background image in each image is the T1 ICBM template. Axial images span z coordinates [-6,0]. D-F. Coronal images of the same probabilistic maps at y = -2.



653

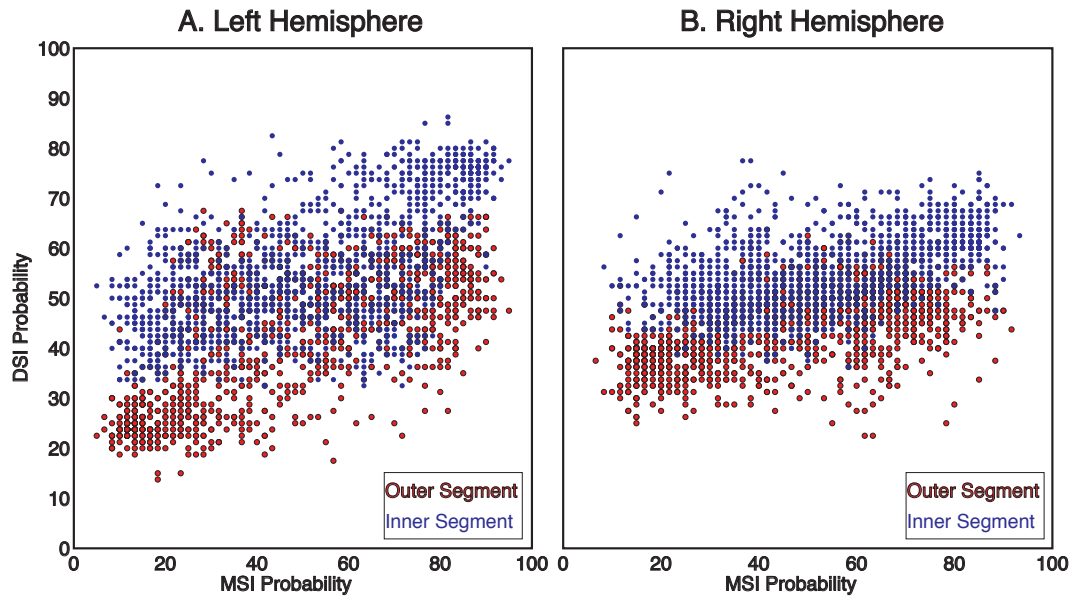
654 Fig. 8

655 A-D. Mean accuracy results from k-means classification in the DSI (A,B) and MSI (C,D)

656 datasets. Dotted lines show random accuracies obtained from 1000 iterations of a

657 permutation test where clustered categories were scrambled. Error bars indicate 95%

658 confidence intervals across subjects.



659

660 Fig. 9

661 The voxelwise MSI probability (averaged across individual subjects) plotted against
662 voxelwise DSI probability for each voxel in the left (A) and right (B) hemispheres. Each
663 point corresponds to an individual voxel in either the outer (red) or inner (blue) segment.